Catalysis Today 174 (2011) 88–96

Contents lists available at ScienceDirect

Catalysis Today

journal homepage: www.elsevier.com/locate/cattod

Synthesis and characterization of nickel ferrite nanocatalysts for CO_2 decomposition

Kuen-Song Lin*, Abhijit Krishna Adhikari, Zong-Yan Tsai, Yu-Pei Chen, Tzu-Ting Chien, Hung-Bin Tsai

Department of Chemical Engineering and Materials Science/Fuel Cell Center, Yuan Ze University, Chung-Li City 320, Taiwan, ROC

ARTICLE INFO

Article history:
Received 26 October 2010
Received in revised form 1 February 2011
Accepted 8 February 2011
Available online 16 March 2011

Keywords:
CO_2 decomposition
Nickel ferrite nanoparticle
Greenhouse effect gas
Methanation
XANES/EXAFS

ABSTRACT

The decomposition of CO_2 over oxygen deficient nickel ferrite nanoparticles (NFNs) at 573 K was studied and fine structures of Fe/Ni species in NFNs catalysts were investigated. Oxygen deficiency of NFNs was obtained by reduction in hydrogen. Decomposition of CO_2 into C and O_2 was carried out within few minutes when it comes into contact with oxygen deficient NFNs through incorporation of O_2 into NFNs. Oxygen and carbon rather than CO were produced in the decomposition process. The complete decomposition of CO_2 was possible because of higher degree of oxygen deficiency and surface-to-volume ratio of NFNs. The pre-edge XANES spectra of Fe atom in NFNs exhibits an absorbance feature at 7115 eV for the 1*s* to 3*d* transition which is forbidden by the selection rule in case of perfect octahedral symmetry. The EXAFS data showed that the NFNs had two central Fe atoms coordinated by primarily Fe–O and Fe–Fe with bond distances of 1.87 and 3.05 Å, respectively. Methane gas was produced during the reactivation of NFNs by flowing H_2. Decomposition of CO_2, moreover, recovery of valuable CH_4 using heat energy of offgas produced from power generation plant or steel industry is an appealing alternative for energy recovery.

© 2011 Elsevier B.V. All rights reserved.

1. Introduction

Carbon dioxide is a highly oxidized and very thermodynamically stable compound, and CO_2 reduction scarcely occurs at room temperature under ambient pressure [1–4]. Carbon dioxide is also of the greatest interest as C_1 feedstock because of the vast amounts and low cost of bulk CO_2. Hydrogenation of CO_2 to produce petrochemical feed stocks, such as oxygenated or hydrocarbons has been extensively explored [2–8], but the high cost of H_2 has limited most applications. Photoreduction of CO_2 has been widely developed into two conceptually different categories that utilize semiconductor electrode/colloid materials [4,5]. Unfortunately, photo-reduction of CO_2 is notoriously inefficient that it has not been recognized as an effective CO_2 utilization alternative [6–10]. The mitigation of CO_2 emission has also been a major environmental concern. One of the most effective solutions may be the in situ decomposition of CO_2 to carbon by catalytic route at lower temperature in each stationary source.

Recently, decomposition of CO_2 to carbon and oxygen over nanophase ferrite catalysts may be an innocent and innovatory technique to reduce greenhouse gas effects [11–14]. Ferrite, a stable and nontoxic material has been widely used in various technical applications including in catalysis. Nanophase ferrites show novel properties that are often significantly different from the bulk due to fundamental changes in coordination, symmetry, and confinement [11–13]. Therefore, the use of nanophase ferrites may lead to not only CO_2 decomposition but also production of CH_4 (methanation) which can be used as an energy source. The dynamic alternation between stoichiometry and non-stoichiometry in spinel ferrites ($M(II)Fe(III)_2O_4$), where M denotes e.g. Ni, Zn, Co, Cu, etc. metal is an important feature that can be exploited in gas reactions. These reactions involve lattice oxygen in two different ways, either through the transfer of oxygen atoms from the ferrite to the gas (oxidation reaction) or through oxygen vacancies being replenished by oxygen from the gas (reduction reaction). The reduction process requires the non-stoichiometric form which can be obtained by the use of a reducing agent such as hydrogen. These non-stoichiometric or oxygen-deficient ferrites can be used to decompose water to hydrogen and carbon dioxide to carbon [15]. Oxygen-deficient ferrites are interesting because of their high decomposition efficiencies for both water and carbon dioxide at low temperatures. Tamaura et al. [15] reported that oxygen-deficient magnetite (Fe_3O_4) decomposes carbon dioxide to carbon with efficiencies up to 100% at low temperature as below 290 °C with the formation of trace amount of carbon monoxide. As the operating temperature is very low, the spinel structure of the ferrite remains stable and able to accommodate interchanges between stoichiometry and non-stoichiometry. Oxygen-deficient ferrites are expressed as $M(II)Fe(III)_2O_{4-\delta}$, where

* Corresponding author. Tel.: +886 34638800x2574; fax: +886 34559373.
E-mail address: kslin@saturn.yzu.edu.tw (K.-S. Lin).

0920-5861/$ – see front matter © 2011 Elsevier B.V. All rights reserved.
doi:10.1016/j.cattod.2011.02.013

δ is the degree of oxygen deficiency. A high δ in magnetite leads to increased Fe^{2+} reduction potentials and enhanced decomposition efficiencies. The M metal influences the reactivities of reduced ferrites toward decomposing carbon dioxide by steering the maximum degree of oxygen-deficiency and thereby the reduction potential of Fe^{2+} [16–19]. Significantly, Kato et al. [16] showed that both the rate of reduction and decomposition are greatly improved when the A metal is Ni^{2+} instead of Fe^{2+}, whereas Tabata et al. [17,18] reported that the opposite is true when the A metal is Mn^{2+}. The valency and fine structure of Ni or Fe atom have not been well studied, though the decomposition of CO_2 has been studied by many groups. The major metal components of the nanophase ferrites are nickel and iron. X-ray absorption spectroscopy (XAS) is an excellent technique for characterizing the valency and local structure of metals in catalysts with short-range order [20,21]. X-ray absorption near edge structure (XANES) spectroscopy provides information of electronic configuration, stereochemistry and the oxidation states of the metallic atoms in nanophase catalysts being investigated. In addition, extended X-ray absorption fine structure (EXAFS) spectroscopy can investigate the information on the atomic arrangement of nanophase catalysts in terms of bond distance, number and kind of near neighbors, thermal and static disorder [20,21]. The XANES and EXAFS also offer the basic knowledge of understanding the oxidation states and fine structures of Ni or Fe in nanophase ferrites to a further study on the mechanism of surface reaction of nanophase ferrites. Thus, the main objectives of the present work were to investigate the conversion efficiency of CO_2 and the fine structures or oxidation states of Ni and Fe species in the nanophase ferrite catalysts.

2. Experimental

2.1. Preparation of nanophase $NiFe_2O_4$

$NiFe_2O_4$ ($Ni_xFe_{3-x}O_{4-\delta}$, $O<\delta<1$) were synthesized by oxidation in air with aqueous suspensions of Fe(II) and Ni(II) hydroxide mixture based on a hydrothermal method. The mixture of nickel sulfate and iron nitrates was neutralized with aqueous ammonia solution until the pH value reached to 8.5. The solution were transferred into a 250 mL PTFE-lined stainless-steel autoclave and heated at 450 K for 4 h. After the hydrothermal reaction, the solid residues of $NiFe_2O_4$ crystals were separated from the solution by centrifugation, washed repeatedly and thoroughly with deionized water, and finally dried at 378 K overnight.

2.2. Decomposition of CO_2

Decomposition of CO_2 was catalyzed by prepared nanophase $NiFe_2O_4$ and the reactions were performed in a continuous flow method using a fixed bed reactor connected to a gas-phase chromatography (GC/TCD, Hewlett-Packard 5890) equipped with a mass sensitive detector. About 1.5–2.0 g $NiFe_2O_4$ was placed in a quartz cell and heated from ambient temperature to 573 K in a hydrogen flow (80 mL min^{-1}) and kept this temperature for 3 h. After flowing with helium (80 mL min^{-1}, 10 min), CO_2 gas (5 mL min^{-1}) was decomposed at 573 K over the reduced NFNs catalyst. The gaseous products, such as CO, CO_2 or CH_4, were detected by GC/TCD. In order to investigate the deactivation of Ni-ferrite catalysts, the durability of bulk and nanophase Ni-ferrites were also conducted over 24 h at 573 K. A Porapak R stainless steel column (80/100, 9.15 mL × 3.175 mm (O.D.)) was programmably heated up at 308 K and held for 11 min and then heated up to 448 K at 30 K min^{-1} to obtain a resolvable separation of CO, CO_2, and CH_4 gases. Helium was used to elute the waste gases for clearing as a carrier gas. In addition, after the CO_2 decomposition, the reactor was flushed again with hydrogen gas to carry out the methanation process and reactivation of the NFNs simultaneously. Methanation process was carried out in order to understand the mechanism of carbon deposition onto NFNs. The quartz cell filled with NFNs was heated up to 573 K in a flowing hydrogen gas (80 mL min^{-1}) and kept this temperature for 2, 4, 6, and 8 h. The outlet gases of methanation onto NFNs were detected by GC/TCD.

2.3. Characterization

X-ray diffraction (XRD) measurements were conducted using standard powder diffraction procedures. The sample was smear-mounted onto a glass slide and then analyzed by Cu Kα radiation (RIGAKU Model D/MAX III-V) at 30 kV and 20 mA with a scan rate of $4^\circ(2\theta)\,min^{-1}$. The specific peak intensities and 2θ values recorded were further identified by a computer database system (JCPDS). FE-SEM (S-4700 Type II) and TEM (Zeiss 10C) were performed to identify the morphologies, crystallinities, and particle size distribution. Nitrogen adsorption isotherms of the samples were measured at 77 K using an ASAP 2010 (Micromeritics). The compositions of gas products for CO_2 decomposition at 573 K over the reduced bulk and NFNs catalysts, such as CO and CO_2, were also analyzed by using an *on-line* FTIR spectroscopy (10-cm gas cell). Infrared spectra were recorded on a Digilab FTIR spectrometer (FTS-40) with fully computerized data storage and data handling capability. For all spectra reported, a 64-scan data accumulation was conducted at a resolution of 4 cm^{-1}. A conventional temperature programmed reduction (TPR) apparatus was used for the investigation of the reducibility of Ni-ferrite catalysts. The TPR measurement was conducted using a flow rate of 30 mL min^{-1} of H_2/Ar mixture (30 vol.% H_2) at 1 atm. A catalyst sample of 0.5 g was tested each time and a heating rate of 10 K min^{-1} was performed from 298 to 650 K.

X-ray absorption (EXAFS and XANES) spectra were collected at the Wiggler beam line 17C1 at NSRRC of Taiwan. The electron storage ring was operated with energy of 1.5 GeV and a current of 100–200 mA. A Si (1 1 1) double-crystal monochromator (DCM) was used for selection of energy with an energy resolution of 1.9×10^{-4}. Data were collected in fluorescence or transmission mode with a Lytle detector [22] in the regions of the Ni (8333 eV) and Fe (7112 eV) K edges at room temperature. The photon energy was calibrated by characteristic pre-edge peaks in the absorption spectra of Ni and Fe standards. The raw absorption data below the edge position were fit to a straight line using the least-square algorithms. The fitted pre-edge background curves were extrapolated throughout all data range, and subtracted and normalized to minimize the effect of sample thickness. The near-edge structure in an absorption spectrum covers the range between the threshold and the point at which the EXAFS begins [23,24]. The k^2 and k^3-weighted and EXAFS spectra were Fourier transformed over the range of interatomic distance (R). The EXAFS data were further analyzed by using the UWXAFS 3.0 program and FEFF 8.0 codes [23,24].

3. Results and discussion

Results from the decomposition of carbon dioxide at 573 K over reduced nanophase and bulk nickel ferrites are shown in Fig. 1. In order to clear demonstration the fast activity rate of NFNs, initial 25 min decomposition has been shown in Fig. 1(a) while the full time decomposition has been shown at inset Fig. 1(b). For both ferites, the highest activity was observed within first 6 min of reaction and thereafter gradually stabilizes at constant levels. After stabilized the decomposition activity, the CO_2 decomposition rate for NFNs was 97–99% while it was about 42% for bulk nickel ferrite and there was no further change was occurred during 18 h for NFNs and 10 h for bulk nickel ferrite. Prior to the CO_2 decomposition both

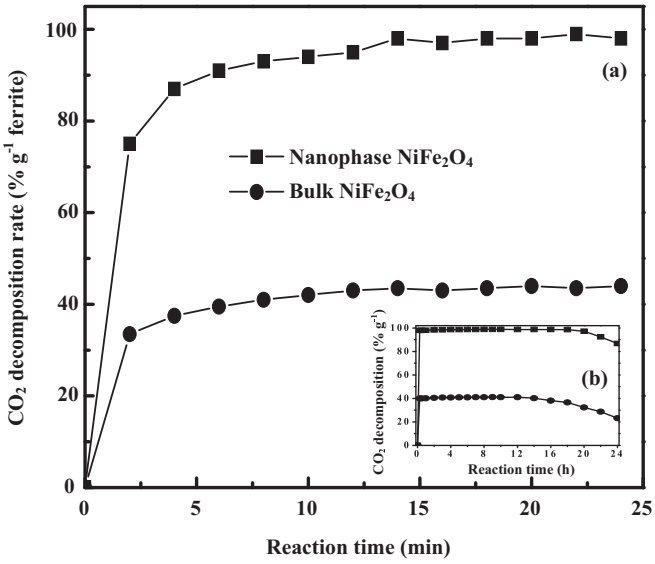

Fig. 1. Decomposition of CO_2 over nanophase $NiFe_2O_4$ and bulk $NiFe_2O_4$ catalysts at 573 K and 1 atm (a) within 25 min and (b) long-term durability test for 24 h (inset).

samples were reduced by hydrogen at the same temperature and time that makes the ferrites more active to adsorb oxygen from CO_2. Due to the slight changes in particle size, CO_2 decomposes into carbon and oxygen within few minutes when it comes into contact with oxygen deficient NFNs. As expected, due to more easy access of oxygen vacancies created by reduction, NFNs with a higher surface area was more reactive to CO_2 decomposition. There are two reaction routes for decomposing CO_2 by oxygen deficient ferrites. One is the decomposition to carbon and oxygen while the other one is decomposition into carbon monoxide and oxygen which can be shown in following equations where δ represents the degree of oxygen deficiency [25–29].

$$\delta/2CO_2 + NiFe_2O_{4-\delta} \rightarrow \delta/2C(s) + NiFe_2O_4 \quad \text{(i)}$$

$$\delta CO_2 + NiFe_2O_{4-\delta} \rightarrow \delta CO + NiFe_2O_4 \quad \text{(ii)}$$

Generally, the reactions take place simultaneously which is reported by different scientists for similar oxygen deficient ferrites [19,25]. Decomposition of CO_2 over oxygen deficient NFNs is stable up to 18 h and decay to 86% after 24 h. For the bulk nickel ferrite, the stable decomposition time is about 10 h. After 24 h the activity of bulk nickel ferrite decreases to 23% only. These results show a very good durability of oxygen deficient NFNs to decompose CO_2 at 573 K and 1 atm. The possible reasons for decay in activity are (i) deposition of carbon on the surface of ferrites that engages the active sites and (ii) deposited carbon on the ferrite surface may partially destroy the spinel structure of ferrites by forming FeC_3 or other intermediate compounds. In our experiments, NFNs produced little or no CO while bulk nickel ferrite resulted in a small amount of undesired CO shown in Fig. 2. The similar pattern for decreasing in CO_2 and evolution of CO could be seen for both ferrites. It can be seen that for oxygen deficient NFNs very few amount of unreacted CO_2 present at the yield while bulk nickel ferrite was not so active to decompose CO_2. Initial concentration of CO_2 was 22.3 mmol L^{-1} and after decomposition the yields were only 0.63 and 12.8 mmol L^{-1} for NFNs and bulk nickel ferrite, respectively. These results suggest that nearly 98–99% of CO_2 was decomposed over oxygen deficient NFNs while this value is about 42% for the bulk nickel ferrite. Thus, the prepared NFNs were more effective to decompose CO_2 into carbon and oxygen than bulk nickel ferrite after reduction by hydrogen because their surface to volume ratio is very high. Komarneni et al. [30] also obtained similar result that

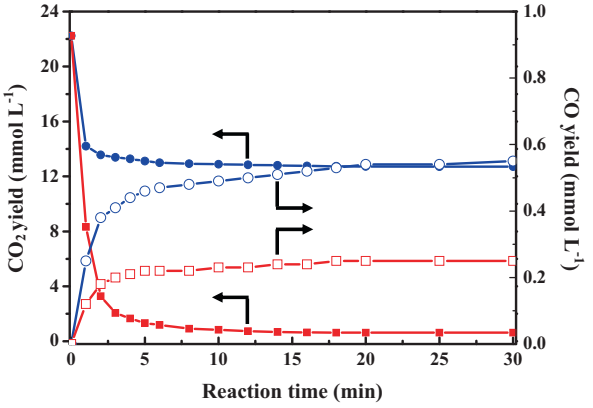

Fig. 2. Concentration variations of CO_2 (solid symbols) and CO (open symbols) yield in the presence of oxygen deficient nanophase (square) and bulk (circle) $NiFe_2O_4$ catalysts at 573 K and 1 atm.

NFNs were more effective than bulk nickel ferrite. FTIR spectra were also performed to demonstrate the yield products qualitatively from the reaction cell operated at 573 K shown in Fig. 3. The FTIR spectra were recorded in 2000–2500 cm^{-1} range with two different temperatures at 573 and 493 K to understand the effects of temperature for decomposing CO_2. The FTIR spectra of NFNs and bulk nickel ferrites have a broad band in the region 2300–2400 cm^{-1} with peak position at 2100–2200 cm^{-1}. The ferrite samples have the bands at 2339 and 2360 cm^{-1} due to δ(O–C–O) and ν_s(O–C–O), respectively. Among 2100–2200 cm^{-1}, the spectra have two bands allotted to C–O bonding. It is assumed that the higher temperature (573 K) is favorable for CO_2 decomposition. The reactivity toward CO_2 decomposition is based on the redox processes of NFNs. If the redox reactions of the ferrite catalysts with H_2 and CO_2 are accelerated in the presence of catalyst, the CO_2 decomposition reactivity of nanophase ferrite can be improved by impregnation of catalyzing metals such as nickel, copper, cobalt, zinc, manganese etc. onto them [26–29]. During the redox reaction, the oxygen atoms of adsorbed CO_2 molecules are incorporated into the oxygen-deficient site of the activated NFNs, and the carbon is deposited on the solid surface to form elementary and/or polymerized carbon.

As shown in Table 1, it shows the comparison between nanophase and bulk nickel ferrite materials. It indicates that NFNs have the surface area of 130 m^2 g^{-1} while bulk nickel ferrite has an average surface area of 15 m^2 g^{-1} only. Therefore, the bulk nickel ferrite was less efficient in CO_2 decomposition than the NFNs. In

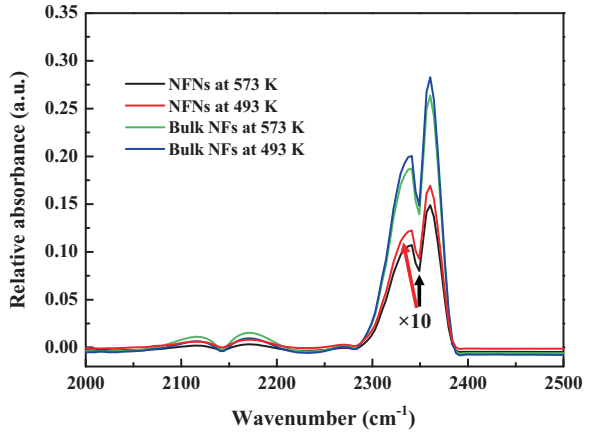

Fig. 3. FTIR spectra of the decomposition of CO_2 over nanophase (ten times scale up of absorbance) and bulk $NiFe_2O_4$ catalysts at 493 K and 573 K under 1 atm. NFNs and NFs denote "nickel ferrite nanoparticles" and "nickel ferrites", respectively.

Table 1
The physicochemical properties of bulk and nanophase nickel ferrite catalysts for CO_2 decomposition at 573 K and 1 atm.

Properties	Bulk $NiFe_2O_4$	Nanophase $NiFe_2O_4$
Partical size (nm)	120–400	15–35
Surface area ($m^2\ g^{-1}$)	8–20	145–170
Shape uniformity	Medium	Good
Reaction activity	Medium	Excellent
Crystallinity of ferrite	Medium	Poor
Selectivity of CO_2 decomposition	0.32–0.41	0.78–0.99

addition, the bulk nickel ferrite led to a higher fraction of CO formation compared to nanophase one. It indicated that the complete decomposition of CO_2 may carried out through the use of NFNs because their surface-to-volume ratio was very high and it was the key point to make more oxygen deficient active catalyst. The mechanism of CO_2 decomposition by the oxygen deficient ferrites is shown in Fig. 4. In principle, when NFNs were treated with hydrogen, they led to the reduction of Fe^{3+} and a charge compensated by ejecting oxygen anions (creation of oxygen vacancies) from the spinel structure. When CO_2 contacts with oxygen deficient ferrites, decomposition of CO_2 occurs by the incorporation of oxygen anions in the vacancies in the oxygen deficient ferrite thereby restoring the ferrite to stoichiometry. At the same time, electrons are donated from the oxygen deficient ferrite to produce carbon or carbon monoxide. Next, the deposited carbon on the surface converts into methane (methanation) upon treatment with H_2 (hydrogenation) while regenerating used ferrite to oxygen deficient ferrite.

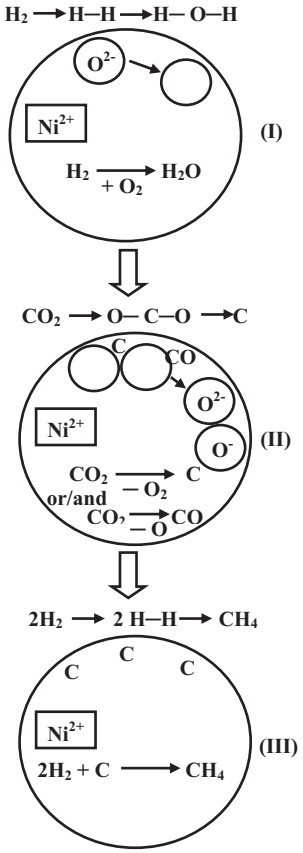

Fig. 4. Symmetric flow diagram of CO_2 decomposition over $NiFe_2O_4$ nanoparticles. (I) H_2 gas decomposes and produces the H_2O molecule which makes oxygen deficient $NiFe_2O_4$, (II) oxygen deficient $NiFe_2O_4$ adsorbs oxygen atoms from CO_2 and produces carbon on the surface or carbon monoxide when $NiFe_2O_4$ is less active, and (III) the produced carbon reacts with H_2 and produces CH_4 by methanation.

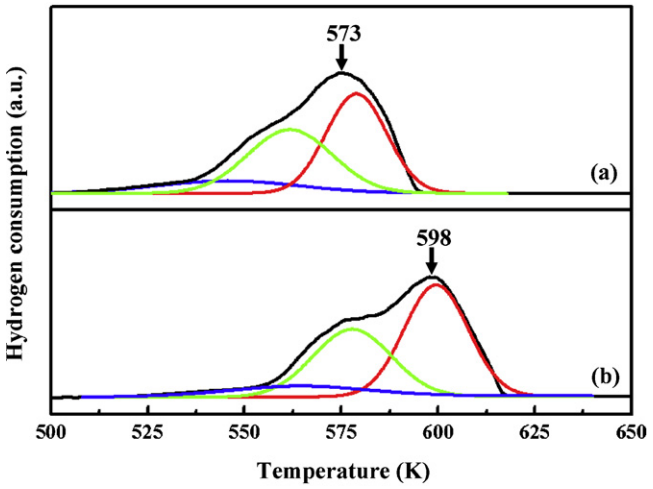

Fig. 5. Hydrogen TPR curves of (a) nanophase and (b) bulk nickel ferrite catalysts for the decomposition of CO_2 at 573 K and 1 atm.

In the second step, carbon monoxide may form instead of carbon when the NFNs were less active or in the other word, when the deficiency of oxygen will be minimized and the structure reached into stoichiometry. The reduction behavior of the NFNs and bulk nickel ferrite are examined by TPR profiles shown in Fig. 5. It can be seen that NFNs showed reduction peaks in lower temperature than bulk nickel ferrite which was probably the results of nanoparticles or higher surface area. The NFNs sample presented broad reduction peak starting at 520 °C and ending at 600 °C. In case of bulk nickel ferrite the reduction peak appeared from 540 to 620 °C. The hydrogen consumption was lower in bulk Ni-ferrite than NFNs which revealed that bulk nickel ferrite was more stable for hydrogenation treatment. It proves that degree of oxygen deficiency obtained in bulk nickel ferrite was lower than NFNs, which showed lower decomposition of CO_2. However, it is assumed that the structure was modified according to the following reaction [31]:

$$ZnFe_2O_4 + H_2 \rightarrow ZnFe_2O_{4-\delta} + \delta H_2O \quad \text{(iii)}$$

The relative oxygen donating ability during hydrogenation determines the activity of the NFNs. Tabata et al. [17] reported that the divalent iron which is formed by reduction acts as the electron donor. Thus, the higher degree of oxygen deficiency or higher content of Fe^{2+} of the NFNs lead to higher degree of conversion of CO_2. Moreover, the δ value for a particular ferrite depends on metal A while the structure can be denoted as AFe_2O_4. Different metal

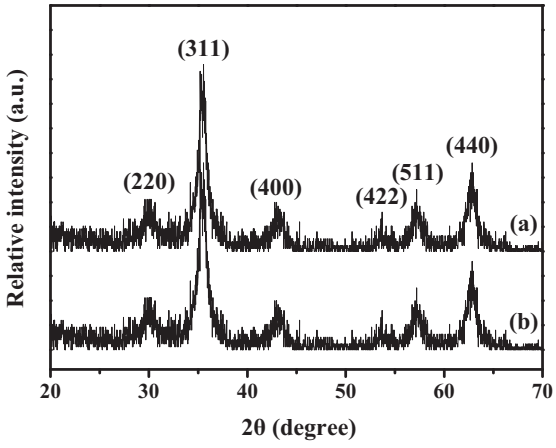

Fig. 6. XRD patterns of (a) fresh and (b) reduced nickel ferrite nanoparticles.

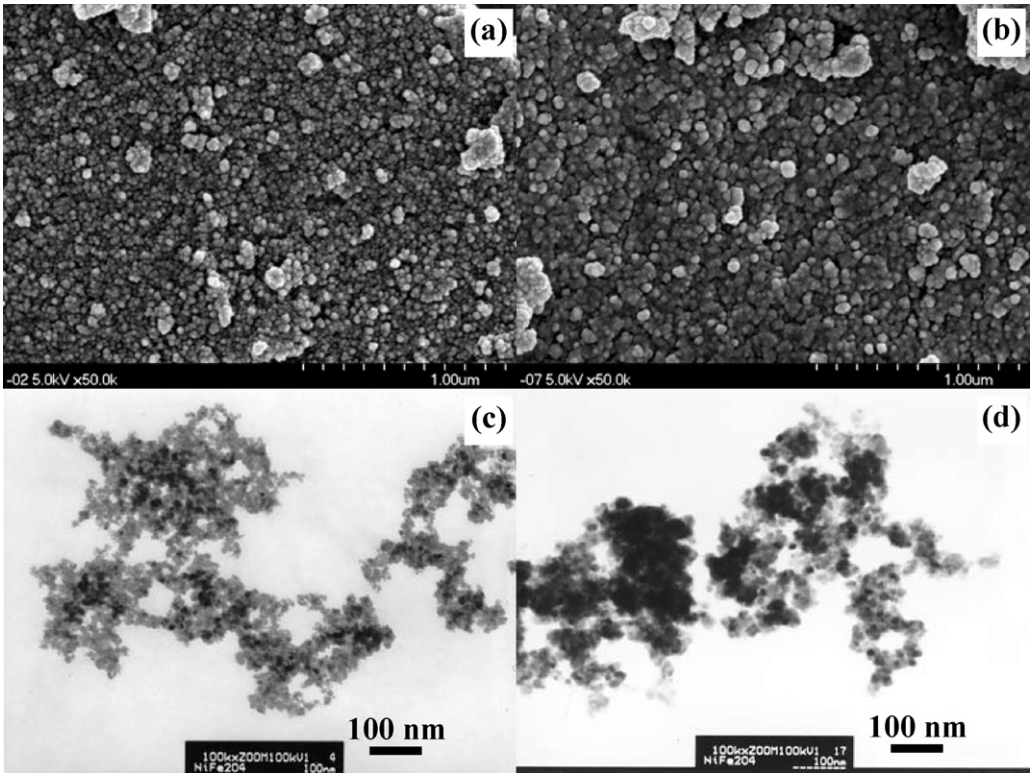

Fig. 7. FE–SEM and TEM micrographs of fresh (a and c) and reduced (b and d) nickel ferrite nanoparticles, respectively for CO_2 decomposition at 573 K and 1 atm.

have different reduction ability to Fe^{3+}. For example, the δ values of nickel and zinc reported as 0.19 and 0.06 by Kodama et al. [19] while 0.58 and 0.16 by Nordhei et al. [29] respectively. The δ value is much higher for nickel metal as it has $3d^8$ orbital while zinc has $3d^{10}$. In this work, we get the δ value for nickel metal is about 0.47 which is lower than the highest possible value. From the viewpoint of energy saving, recovery of valuable methane by decomposition of CO_2 over NFNs with recycling heat energy of offgas produced from plants is also an appealing resource recovery alternative in the future.

CO_2 is a stable molecule. Both terms of Gibbs free energy disadvantage the conversion of CO_2 into other products. The C=O bond of CO_2 molecules are quite stable and an important heat energy input must be supplied to make their dissociation possible. For $2CO_2 \rightarrow 2CO + O_2$ reaction, ΔH° is 569 kJ mol^{-1} at atmospheric pressure and 298 K [32]. This reaction is not product favorable and this heat energy supply makes the reaction economically not feasible. However, as the system can be incorporated as an integrated part with exhaust gases of incineration/combustor in power plants or other industries (e.g. steel, petroleum or refinery), heat energy can be supplied from hot exhaust gases. Furthermore, there is another cost remains for separation/purification processes to recover CH_4 from product gases. It is expected that the separation/purification cost would not be exceeded than the energy cost recovered from the produced CH_4. Based on the overall drawbacks and advantages of the process, it can be attributed that, the implementation of this process at the exhaust of any industry from where it will recover the heat energy would be economically feasible.

The direct methanation of CO_2 based on different catalysts is also investigated by many researchers [33–35]. However, the conversion rate of CO_2 in presence of catalysts was only 21% at 423 K, 41–80% at 673 K and 60–78% at 773 K reported by Jacquemin et al. [33], Ocampoa et al. [34] and Sivaiah et al. [35], respectively. Based on these results, it can be seen that, the prepared NFNs catalyst in this work is more active to decompose CO_2 when it is activated by hydrogenation through ejecting the oxygen atoms from the spinel structure.

The XRD patterns of the fresh and reduced NFNs materials are plotted in Fig. 6(a) and (b) respectively. Both fresh and reduced samples are crystalline as they show sharp diffraction peaks, and the position and relative intensity of the diffraction peaks of the sample match well with the standard XRD data for spinel nickel ferrite (JCPDS file No. 10-0325). Moreover, the diffraction peaks of our sample prepared in this study matched well with the already published XRD patterns on the same NFNs [26,36,37]. The intensive peaks appearing at 2θ angles in the XRD pattern of NFNs are characteristics of porous materials which possess numerous pores or cavities. It can be seen that the structure remain spinel after the reduction process. It was observed that the diffraction peaks for both fresh and reduced NFNs materials corresponding to (2 2 0), (3 1 1), (4 0 0), (4 2 2), (5 1 1), and (4 4 0) diffraction planes of NFNs were present [38]. A spinel can be represented by the formula AB_2O_4, the A–B magnetic interactions between the magnetic atoms on the A (tetrahedral) site and the B (octahedral) sites are stronger than A–A interactions and B–B interactions. That is, nanophase $NiFe_2O_4$ crystallizes in the spinel structure which contains two different cation sites: eight tetrahedral A sites and 16 octahedral B sites. From the XRD data, in the lattice of NFNs with a completely inverse-spinel structure, an equal number of the Fe cations are at the tetrahedral and octahedral sites, respectively. The recoiless fractions of Fe nucleus at the tetrahedral and octahedral sites are nearly equal. The oxygen-deficient ferrite synthesized by activation of spinel ferrite with H_2 at 573 K was represented by $Ni_xFe_{3-x}O_{4-\delta}$ ($O \leq x \leq 1$, $\delta > 0$) where δ denoted the oxygen deficiency. The average crystallite size of NFNs is calculated to be 21 nm using Scherrer formula from the (3 1 1) plane (which corresponds the strongest peak). The particle size of synthesized NFNs and reduced NFNs were around 10–30 nm and 15–40 nm identified by FE-SEM micrographs shown in Fig. 7(a) and (b), respectively. The fresh NFNs were well dispersed and spherical in shape with irregular size. However, the

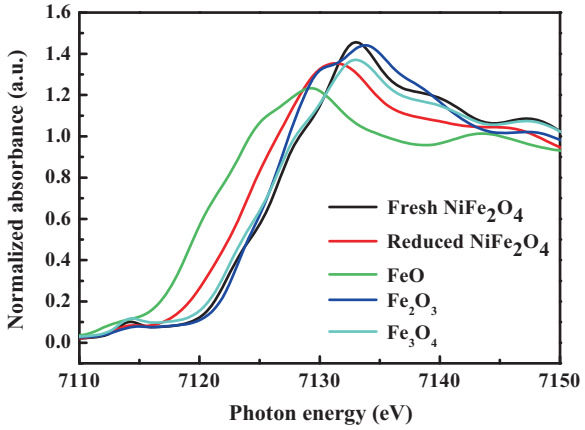

Fig. 8. Normalized Fe K-edge XANES spectra of fresh nanophase $NiFe_2O_4$, reduced $NiFe_2O_4$ nanoparticle, FeO, Fe_3O_4, and Fe_2O_3 standards.

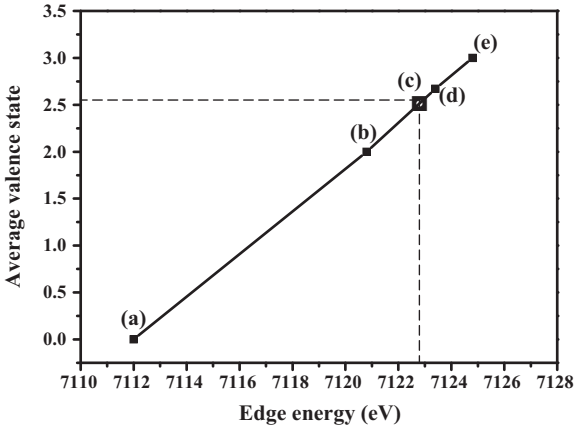

Fig. 9. Edge energies of (a) Fe metal, (b) FeO, (c) reduced $NiFe_2O_4$, (d) Fe_3O_4, and (e) Fe_2O_3 as a function of the average valence state.

reduced NFNs were also in spherical shape with a little bigger diameter. It may attribute, in higher reduction temperature the samples aggregated and thus gives the bigger diameter than that of fresh NFNs. This phenomenon also revealed from extensive TEM examinations shown in Fig. 7. The TEM images of fresh and reduced NFNs samples are shown in Fig. 7(c) and (d), respectively, where it can be seen that the particle size of the reduced sample is little bit bigger than that of fresh NFNs. The TEM images revealed that the particle size of the fresh NFNs were about 10–25 nm while the range was larger for reduced NFNs.

The normalized Fe K-edge XANES of fresh and reduced nickel ferrites with the FeO, Fe_2O_3, and Fe_3O_4 standards are represented in Fig. 8. The Fe absorption K-edge shifts to lower energies upon reduction in hydrogen which is consistent with a reduction in the average valence state of Fe^{3+}. Removing oxygen from the spinel structure of $NiFe_2O_4$ mainly influences the valence state of iron with the shift being largest for NFNs. The pre-edge XANES spectra of Fe in NFNs exhibit an absorbance feature (7115 eV) for the 1*s* to 3*d* transition which was forbidden by the selection rule in the case of perfect octahedral symmetry. The sharp feature at 7134 eV, due to the dipole-allowed of 1*s* to $4p_{xy}$ electron transition, indicated the existence of Fe^{3+}. The intensity of the 1*s* to $4p_{xy}$ transition was proportional to the population of Fe^{3+} in NFNs. Due to the reduction in the flowing hydrogen, a shoulder at 7121 eV and an intense feature at 7126 eV were attributed to the 1*s* to $4p_{xy}$ transition that indicated the existence of Fe^{2+} species in reduced NFNs catalysts. Oxygen and nickel are the major atoms coordinated to the two central Fe atoms in fresh nanophase ferrites. The edge energies of the four references FeO, Fe_2O_3, Fe_3O_4, and iron metal as 2, 3, 2.67, and 0, respectively were plotted against their average valence state shown in Fig. 9. This plot was used to estimate the valence states of iron species in the reduced ferrites as it displays a linear relationship between the edge energy and valence state as exemplified by the reduced NFNs (Fig. 9(c)). The edge energies (±0.5 eV) were defined as being half the edge height. The local environments in the oxide references and the ferrites are similar; hence the contribution from the chemical shifts to the absorption edges is also similar. As the iron atoms are in both Fe^{2+} and Fe^{3+} valence states, the spinel Fe_3O_4 is especially appropriate as a reference. Therefore, it is valid to use Fig. 9 to ascertain the valence states of the reduced NFNs. The degree of oxygen deficiency was estimated from the decrease in average valence state of iron species. It was assumed that the spinel structure of NFNs $(Ni(II)Fe(III\text{-}d)_2O_{4-\delta}$ was maintained and hence charge neutrality was taking into account to obtain the oxygen deficiency. Valence state of iron reflects the loss of oxygen from the spinel structure and by taking into account this phenomenon we get the δ value for the reduced NFNs is 0.47 and the estimated chemical formula is $NiFe_2O_{3.53}$.

The NFNs were further studied by using EXAFS to understand the fine structure and the behavior in the decomposition of carbon dioxide. Fe K-edge EXAFS spectroscopy can also provide the information on the Fe atomic arrangement of catalysts in terms of bond distance, number, and kind of near neighbors. Fig. 10 shows the k^3-weighted and least-square fitted Fe K-edge EXAFS and their Fourier transforms of fresh (Fig. 10(a–b)) and reduced (Fig. 10(c and d)) NFNs, respectively. Since, XANES shows significant changes between fresh and reduced NFNs, it is interesting that the EXAFS data shown in Table 2 are virtually identical. It shows that the NFNs have two center Fe atoms coordinated by primarily Fe–O and Fe–Fe bonding. The fine structural parameters of NFNs analyzed by the EXAFS data also suggested that Fe atoms in NFNs may be mirror-symmetrically (D_d) surrounded by two Ni atoms and four oxygen atoms. The EXAFS data also showed that the fresh NFNs had two central Fe atoms coordinated by primarily Fe–O and Fe–Fe with bond distances of 1.87 ± 0.02 Å and 3.05 ± 0.02 Å with the coordination number of 5.6 and 4.3, respectively. After the reduction, the bond distances of Fe–O and Fe–Fe changes into 1.89 ± 0.02 Å and 3.09 ± 0.02 Å, respectively. This is a statistical effect; this means that in spite of removing a small amount of oxygen atoms from the lattice, the overall structure is maintained with little electronic changes. In contrast to the Fe K-edge, the Ni K-edge Fourier transforms of fresh (Fig. 11(a and b)) and reduced NFNs (Fig. 11(c and d)) show significant differences. Minor amounts of nickel metal are

Table 2
Fine structural parameters of fresh and reduced $NiFe_2O_4$ nanoparticles analyzed by using EXAFS at Fe and Ni K-edges.

Shell		CN[a] (±0.05)	R[b] (±0.02 Å)	$\Delta\sigma^2$ (Å²)[c]
Fresh $NiFe_2O_4$				
Fe–O	1st	5.74	1.87	0.006
	2nd	2.06	2.01	0.008
Fe—Fe	1st	4.31	3.05	0.012
	2nd	5.72	4.34	0.018
Ni–O	1st	4.04	1.99	0.005
Reduced $NiFe_2O_4$				
Fe–O	1st	5.48	1.89	0.005
	2nd	1.92	2.05	0.011
Fe—Fe	1st	4.09	3.09	0.010
	2nd	5.18	4.37	0.019
Ni–O	1st	3.83	2.00	0.006

[a] Coordination number.
[b] Bond distance.
[c] Debye–Waller factor.

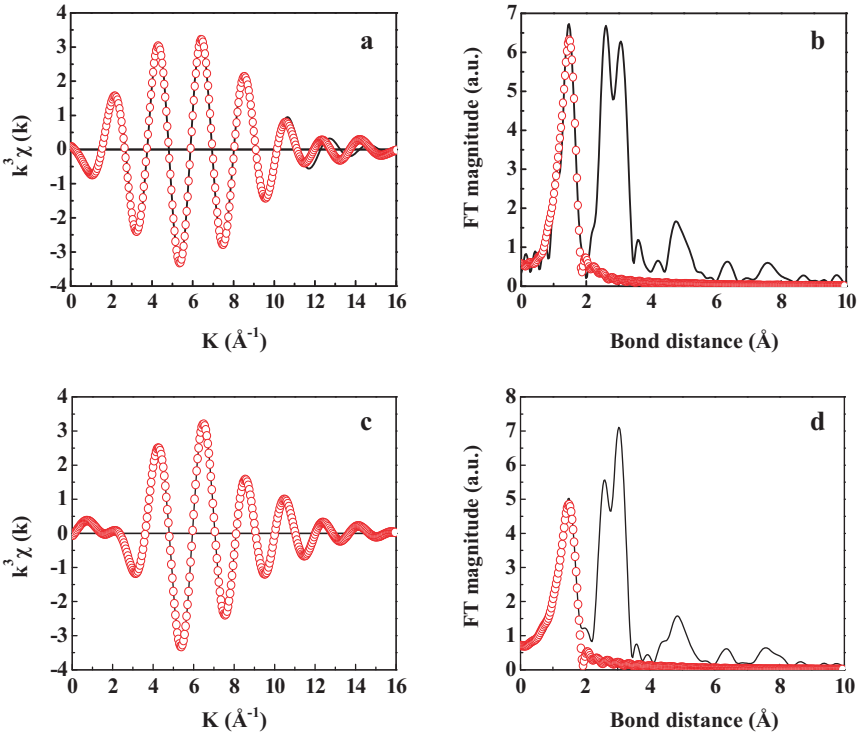

Fig. 10. Fe K-edge EXAFS oscillation k^3 (k) and Fourier transform (FT) spectra of (a and b) fresh nanophase $NiFe_2O_4$ and (c and d) reduced $NiFe_2O_4$ nanoparticles, respectively. The best fitting of the EXAFS spectra are expressed by the dotted lines.

formed after reduction. Moreover, the bond length of Ni–O of fresh NFNs is 1.99 ± 0.02 Å while it is 3.83 ± 0.02 Å for the reduced NFNs shown in Table 2. The lack of any structural changes confirms that the spinel structure is maintained after reduction, even though a minor amount of nickel metal is formed. Hence, the EXAFS suggests that over reduction does not lead to a complete disintegration of the structure but rather to ejection of metal from the oxygen deficient spinel. These results are similar to those reported by Zhang et al. [39] where the oxygen-deficiency is constant regardless of the quantity of metal formed. Importantly, this means that, in spite

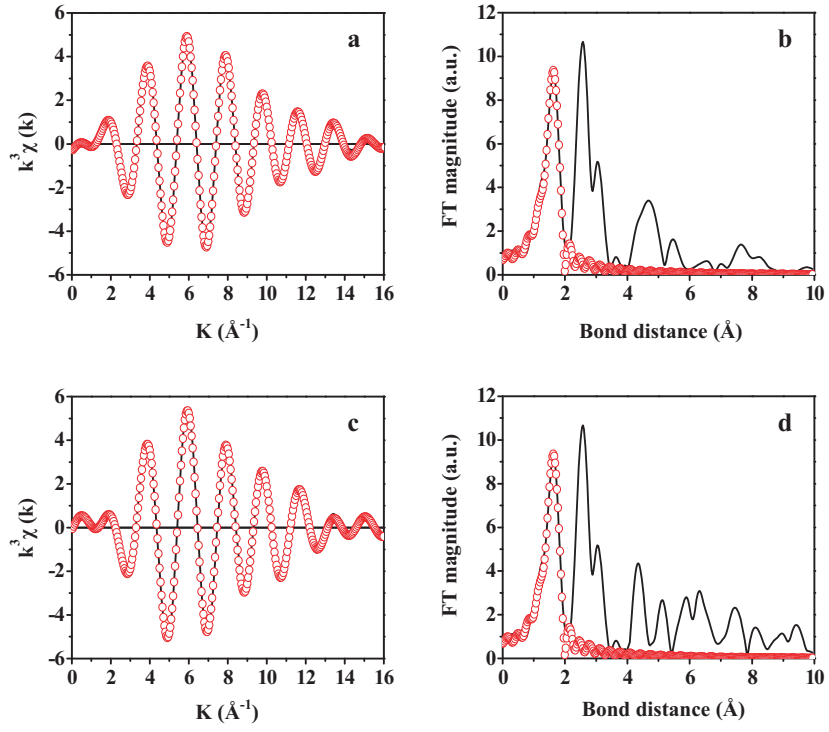

Fig. 11. Ni K-edge EXAFS oscillation k^3 (k) and Fourier transform (FT) spectra of (a and b) fresh nanophase $NiFe_2O_4$ and (c and d) reduced $NiFe_2O_4$ nanoparticles, respectively. The best fitting of the EXAFS spectra are expressed by the dotted lines.

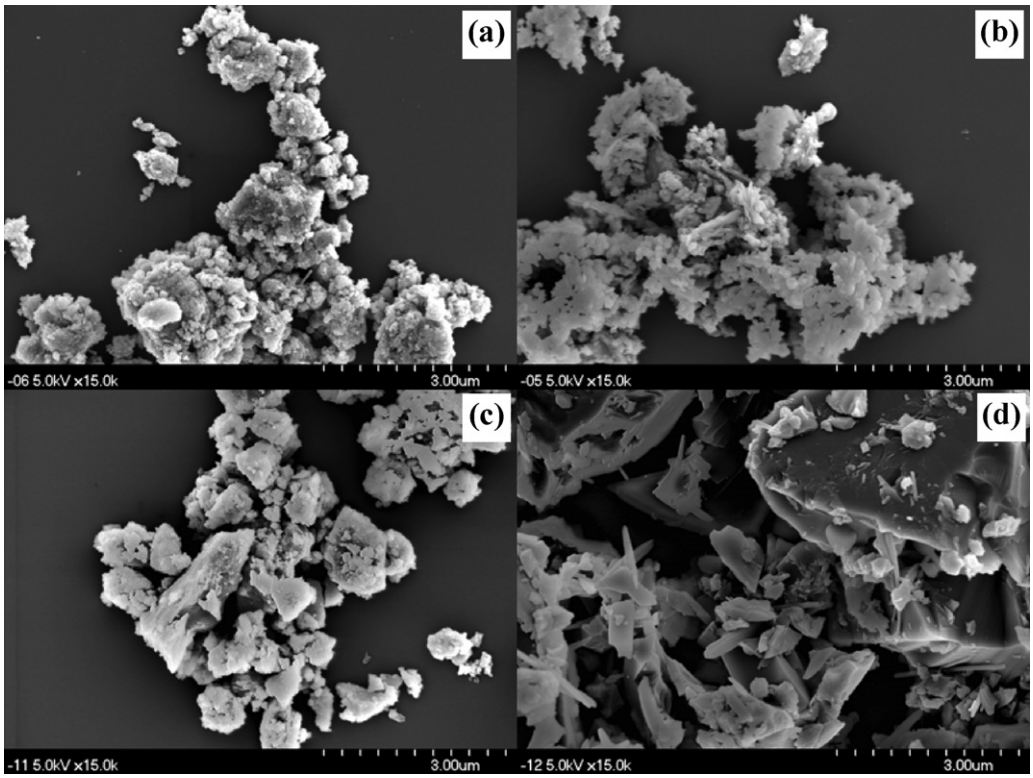

Fig. 12. FE-SEM micrographs of $NiFe_2O_4$ nanoparticles after (a) 2, (b) 4, (c) 6, and (d) 8 h of methanation.

of over-reduction, the material is still active in the reaction with carbon dioxide.

The FE-SEM images of the reduced NFNs during reactivated or hydrogenated at different time interval of 2, 4, 6, and 8 h were shown in Fig. 12. It can be seen that at the beginning of reduction process the surface of the NFNs is covered by whether carbon or the intermetallic compounds formed by produced carbon and the expelled nickel metal from the structure. As the reduction time increased, the amount of the carbon or the intermetallic compounds removed due to the methanation process. The decomposition of CO_2 by the 6 h reactivated NFNs showed good result with more than 90% decomposition rate. Interestingly, the particle size also increased. It might happen due to the aggregation of the particles at that higher temperature of 573 K.

4. Conclusions

From XRD pattern, NFNs having the smaller particle sizes and lower crystal structure showed a relatively broad peak. TEM photographs also showed fine spherical features of the NFNs with the diameters ranged of 10–25 nm. The NFNs were all separated and the sizes were narrowly distributed. Due to the slight changes in particle sizes, CO_2 decomposes into carbon and oxygen within few minutes when it comes into contact with oxygen deficient NFNs. As expected, due to more easy access of oxygen vacancies created by reduction, NFNs with a higher surface area were more reactive to CO_2 decomposition. In addition, the bulk nickel ferrite led to a higher fraction of CO compared to nanophase one. It indicated that the complete decomposition of CO_2 is possible through the use of NFNs because of their higher surface-to-volume ratio and higher degree of oxygen deficiency. The pre-edge XANES spectra of Fe species in NFNs exhibit an absorbance feature (7115 eV) for the 1*s* to 3*d* transition which is forbidden by the selection rule in the case of perfect octahedral symmetry. The EXAFS spectra also showed that the NFNs had two central Fe atoms coordinated by primarily Fe–O and Fe–Fe with bond distances of 1.87 Å and 3.05 Å, respectively. The recovered methane during reactivation of NFNs by hydrogenation can be used as energy source. As this process requires heat energy, it can be used at the exhaust of power plant or other industry to get the heat energy without further cost to make the process economically feasible.

Acknowledgements

The financial support of the National Science Council, Taiwan (NSC-94-2211-E-155-001) is gratefully acknowledged. We also thank Prof. Y.W. Yang and Dr. J.F. Lee of the Taiwan Synchrotron Radiation Research Center (NSRRC) for their helps in the EXAFS experiments.

References

[1] F. Joos, G.K. Plattner, T.F. Stocker, A.K. Schmittner, Science 284 (1999) 464–467.
[2] P.G. Jessop, R. Noyori, Chem. Rev. 95 (1995) 259–272.
[3] Y. Borodko, G.A. Somorjai, Appl. Catal. A 186 (1999) 355–362.
[4] N. Nomura, T. Tagawa, S. Goto, Appl. Catal. A 166 (1998) 321–326.
[5] D. Li, N. Lchikuni, S. Shimazu, T. Uematsu, Appl. Catal. A 180 (1999) 227–235.
[6] H.Y. Wang, C.T. Au, Appl. Catal. A 155 (1997) 239–252.
[7] S. Wang, G.Q. Lu, Appl. Catal. A 169 (1998) 271–280.
[8] M. Yamasaki, M. Komori, E. Akiyama, H. Habazaki, A. Kawashima, K. Asami, K. Hashimoto, Mater. Sci. Eng. A 267 (1999) 220–226.
[9] J.-Y. Wang, G.-G. Xia, A. Huang, S.L. Suib, Y. Hayashi, H. Matsumoto, J. Catal. 185 (1999) 152–159.
[10] S. Furukawa, M. Okada, Y. Suzuki, Energy Fuels 13 (1999) 1074–1081.
[11] M. Tsuji, Y. Wada, T. Yamamoto, T. Sano, Y. Tamaura, J. Mater. Sci. Lett. 15 (1996) 156–158.
[12] J.W. Choung, Z. Xu, J.A. Finch, Ind. Eng. Chem. Res. 38 (1999) 4689–4693.
[13] A.J. Rondinone, A.C.S. Samia, Z.J. Zhang, J. Phys. Chem. B (2000) 7919–7922.
[14] H.Y. Luo, Z.X. Yue, Y.J. Zhou, J. Magn. Magn. Mater. 210 (2000) 104–108.
[15] Y. Tamaura, M. Tabata, Nature 346 (1990) 255–256.
[16] H. Kato, T. Kodama, M. Tsuji, Y. Tamaura, S.G. Chang, J. Mater. Sci. 29 (1994) 5689–5692.
[17] M. Tabata, Y. Nishida, T. Kodama, K. Mimori, T. Yoshida, Y. Tamaura, J. Mater. Sci. 28 (1993) 971–974.

[18] M. Tabata, K. Akanuma, K. Nishizawa, K. Mimori, T. Yoshida, M. Tsuji, Y. Tamaura, J. Mater. Sci. 28 (1993) 6753–6760.
[19] T. Kodama, M. Tabata, T. Sano, M. Tsuji, Y. Tamaura, J. Solid State Chem. 120 (1995) 64–69.
[20] G. Meitzner, G.H. Via, F.W. Lytle, J.H. Sinfelt, J. Phys. Chem. 96 (1992) 4960–4964.
[21] S.I. Zabinsky, J.J. Rehr, A. Ankudinov, R.C. Albers, M.J. Eller, Phys. Rev. B 52 (1995) 2995–3009.
[22] F.W. Lytle, J. Synchrotron Radiat. 6 (1999) 123–134.
[23] T. Resslert, J. Synchrotron Radiat. 5 (1998) 118–122.
[24] A.I. Nesvizhskii, J.J. Rehr, J. Synchrotron Radiat. 6 (1999) 315–316.
[25] M. Tabata, K. Akanuma, T. Togawa, M. Tsuji, Y. Tamaura, J. Chem. Soc. Faraday Trans. 90 (1994) 1171–1175.
[26] P.P. Sarangi, S.R. Vadera, M.K. Patra, N.N. Ghosh, Powder Technol. 203 (2010) 348–353.
[27] H.-C. Shin, S.-C. Choi, K.-D. Jung, S.-H. Han, Chem. Mater. 13 (2001) 1238–1242.
[28] C. Nordhei, K. Mathisen, O. Safonova, W. van Beek, D.G. Nicholson, J. Phys. Chem. C 113 (2009) 19568–19577.
[29] C. Nordhei, K. Mathisen, I. Bezverkhyy, D. Nicholson, J. Phys. Chem. C 112 (2008) 6531–6537.
[30] S. Komarneni, M. Tsuji, Y. Wada, Y. Tamaura, J. Mater. Chem. 7 (1997) 2339–2340.
[31] M.A. Valenzuela, P. Bosch, J. Jiménez-Becerrill, O. Quiroz, A.I. Páez, J. Photochem. Photobiol. A 148 (2002) 177–182.
[32] A.K. De, A Text Book of Inorganic Chemistry, ninth ed., New Age International, New Delhi, 2007.
[33] M. Jacquemin, A. Beuls, P. Ruiz, Catal. Today 157 (2010) 462–466.
[34] F. Ocampoa, B. Louisa, L. Kiwi-Minskerb, A.C. Rogera, Appl. Catal. A 392 (2011) 36–44.
[35] M.V. Sivaiah, S. Petit, M.F. Beaufort, D. Eyidi, J. Barrault, C. Batiot-Dupeyrat, S. Valange, Micropor. Mesopor. Mater. 140 (2011) 69–80.
[36] C. Nordhei, A.L. Ramstad, D.G. Nicholson, Phys. Chem. Chem. Phys. 10 (2008) 1053–1066.
[37] J.-S. Kim, C.-W. Ham, Mater. Res. Bull. 44 (2009) 633–637.
[38] A. Verma, T.C. Goel, R.G. Mendiratta, M.I. Alam, Mater. Sci. Eng. B 60 (1999) 156–162.
[39] C.L. Zhang, S. Li, L.J. Wang, T.H. Wu, S.Y. Peng, Mater. Chem. Phys. 62 (2000) 44–51.